引用格式：XUE Ting, HUANG Jianliang, YAN Shaolong, et al. Mid Wavelength Interband Cascade Photodetector with Type Ⅱ Superlattice Absorber (Invited)[J]. Acta Photonica Sinica, 2023, 52(10):1052405
薛婷,黄建亮,鄢绍龙,等.基于Ⅱ类超晶格的中波红外带间级联探测器(特邀)[J].光子学报,2023,52(10):1052405

基于Ⅱ类超晶格的中波红外带间级联探测器（特邀）

薛婷[1,2],黄建亮[1,2],鄢绍龙[1,2],张艳华[1,2],马文全[1,2]
(1 中国科学院半导体研究所 半导体材料科学重点实验室,北京 100083)
(2 中国科学院大学 材料与光电研究中心,北京 100049)

摘　要：为了提高红外探测器的工作温度，基于InAs/GaSb Ⅱ类超晶格材料设计了一种五级带间级联结构中波红外光电探测器，并采用分子束外延技术和标准化光刻及刻蚀技术进行了器件的制备。在77 K时，该器件的50%截止波长是4.02 μm，在0 V时峰值探测率为1.26×10^{12} cm·$Hz^{1/2}$/W；在300 K零偏压下，该器件的50%截止波长是4.88 μm，峰值探测率为1.28×10^{9} cm·$Hz^{1/2}$/W，实现了高温探测。从180 K到300 K，器件的暗电流主要由扩散电流主导。在77 K到220 K温度范围的暗电流曲线中观察到了负微分电阻现象，并解释了峰谷电流比相对于温度变化的趋势。研究结果表明，具有带间级联结构的T2SL探测器可以进行室温工作，在中波范围内有比较明显的优势。

关键词：半导体探测器；中波；分子束外延；带间级联探测器；InAs/GaSb超晶格
中图分类号：TL814　　**文献标识码**：A　　**doi**：10.3788/gzxb20235210.1052405

0　引言

红外探测器在气象探测、医疗诊断、对地观测、夜视安防以及预警与跟踪等领域有重要的应用价值。目前市场上的高性能红外探测器有碲镉汞(Mercury Cadmium Telluride,MCT)和量子阱探测器等。其中MCT探测器具有带隙可调、量子效率高、复合暗电流低等优点，但成本高；量子阱探测器成本低，但量子阱材料基于子带间跃迁吸收，量子效率低，而且因为不能吸收垂直入射光，需要制作表面光栅，增加了器件工艺成本。近年来，InAs/GaSb Ⅱ类超晶格(T2SL)得到了广泛关注。T2SL的有效带隙取决于电子和空穴形成的微带，通过调节InAs层和GaSb层的厚度可以灵活调节带隙实现约1～32 μm的探测，因为是带间跃迁，其量子效率远高于量子阱；而且，在Ⅱ类超晶格结构中，因为轻重空穴分离，降低了俄歇复合率；同时，由于电子有效质量高，降低了隧穿暗电流[1]。基于此材料，科研人员已经成功实现了短波[2-5]、中波[6-8]、长波[9-11]和甚长波[11,13]的红外探测。但T2SL探测器通常要在低温下工作，需要制冷，这大大增加了整机尺寸、功耗和成本。为了降低探测器的暗电流，不同势垒能带结构的T2SL探测器被提出，如采用单极势垒[14-15]、互补势垒[11]、M结构势垒[16]、双异质结构[17]的探测器，以及带间级联结构红外探测器[9,18]。

2005年，LI J V和YANG R Q采用了与带间级联激光器(Interband Cascade Laser,ICL)[19-20]相同的结构制备出了带间级联探测器(Interband Cascade Infrared Photodetectors, ICIP)[21]，接近当时商用PbSe光电探测器的探测率水平。2010年，YANG R Q采用InAs/GaSb二类超晶格作为吸收区，报道了室温下截止波长为7 μm的带间级联探测器，室温下探测率达到4.5×10^{8} cm·$Hz^{1/2}$/W[22]。KRISHNA S课题组在2012年制备了七级带间级联中波探测器，295 K时100%截止波长是6.2 μm，探测率为8.9×10^{8} cm·$Hz^{1/2}$/W[23]。该课题

基金项目：国家自然科学基金面上项目(No. 61874103)
第一作者：薛婷，xueting@semi.ac.cn
通讯作者：黄建亮，jlhuang@semi.ac.cn；马文全，wqma@semi.ac.cn
收稿日期：2023-06-28；**录用日期**：2023-08-25

组在2014年制备了五级带间级联探测器焦平面阵列(Interband Cascade Photodetector Focal Plane Array, IC FPA),在300 K时50%截止波长为4.4 μm,最高工作温度为180 K[24]。近年来,科研人员将不同的材料与ICIP结构结合。中国科学院上海技术物理研究所制备了InAs基的中波ICIP[25-26],在300 K时,两级和三级带间级联探测器的探测率分别是2.23×10^{8} cm·Hz$^{1/2}$/W和1.94×10^{8} cm·Hz$^{1/2}$/W。德国科学家BADER A设计并制备了以Ga-free超晶格材料作为吸收区的ICIP,目的是将InAs/InAsSb材料的Ⅱ类超晶格材料的优点与带间级联结构的优点结合起来,但因为受到材料少数载流子扩散长度的限制,峰值探测率在300 K只有约10^{8} cm·Hz$^{1/2}$/W[27]。由以上结果可知,ICIP在高温工作条件下的表现优于单级吸收区探测器。这是因为普通单级探测器在高温时扩散长度变小,量子效率降低,而ICIP的分级结构使得扩散长度大于每一级吸收区,从而避免了高温下变短的扩散长度带来的响应率的减小;同时,由于带间级联结构中存在高带隙的AlSb材料,且是多个结构之间串联,提高了电阻,这可能会进一步降低暗电流[28]。

基于带间级联结构在高温工作的优势,本文采用T2SL材料作为吸收区设计并制备了一个五级带间级联中波红外光电探测器,相比于其他带间级联探测器,该器件在达到相似探测率水平下截止波长更长。且在77~220 K温度范围的暗电流曲线中观察到了负微分电阻效应(Negative Differential Resistance, NDR),对峰谷电流比随温度升高而降低的趋势进行了解释。

1 结构设计及生长

如图1所示,带间级联探测器采用多级级联结构,每级由吸收区、空穴势垒区和电子势垒区组成,吸收区多采用InAs/GaSb二类超晶格,空穴势垒区一般采用InAs/AlSb多量子阱,电子势垒区一般采用GaSb/AlSb多量子阱。吸收区位于空穴势垒区和电子势垒区之间,吸收光子能量产生电子,电子向电子势垒区的运输被高势垒阻挡,但可以在光学声子的辅助下弛豫到最低能级,再通过电子势垒区共振隧穿到下一吸收区的价带,完成带间级联输运过程。

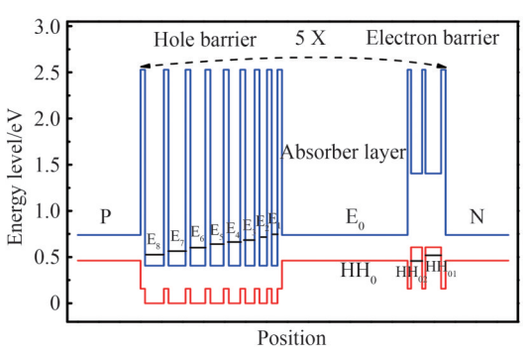

图1 探测器的能带结构示意图

Fig. 1 Schematic drawing of the band structure of the detector

在带间级联结构中,空穴势垒区的能级E_1应与吸收区的电子基态能级E_0接近,电子势垒区的空穴能级HH_{02}应与吸收区的重空穴能级HH_0接近,相邻能级之间的弛豫和隧穿需要光学声子的辅助,所以空穴势垒区和电子势垒区的能级应设计为等差分布,相邻能级之间的能量差应为一个纵向光声子能量,约为30 meV。

基于以上原理,采用8 k·p模型对能带结构进行计算并对探测器中的级联结构能级进行设计,其中以InAs材料的价带顶为能量零点。为了实现中波红外探测,吸收区采用InAs(2.4 nm)/GaSb(3.6 nm)超晶格结构,厚度为0.5 μm,对应的电子基态E_0和重空穴基态HH_0分别约为0.72 eV和0.43 eV。该探测器利用了从HH_0到E_0的跃迁,因此吸收区的有效带隙为0.29 eV,对应的探测波长就是4.28 μm。为了光生载流子输运,空穴势垒区由AlSb(2.1 nm)/InAs(9.0 nm)/AlSb(2.2 nm) /InAs(8.1 nm)/AlSb(2.3 nm)/InAs(7.2 nm)/AlSb(2.4 nm)/InAs(6.3 nm)/AlSb(2.5 nm)/InAs(5.4 nm)/AlSb(2.4 nm)/InAs(4.5 nm)/AlSb(2.3 nm)/InAs(3.6 nm)/AlSb(2.2 nm) /InAs (2.9 nm) /AlSb(2.1 nm)组成,其对应的电子能级(E1、E2、E3、E4、E5、E6、E7、E8)的差约等于一个纵向光学声子的能量。电子势垒区由两个空穴量子阱组成,具体排列是AlSb(2.1 nm)/GaSb(5.3 nm)/AlSb(2.1 nm)/GaSb(7.5 nm)/AlSb(2.1 nm),计算得到相邻能级的能量差与纵向

光学声子能量有轻微偏差，但基本符合设计。

P型接触层为0.5 μm厚的GaSb和100个周期的InAs（2.4 nm）/GaSb（36 nm）超晶格，掺杂浓度为2×10^{18} cm^{-3}；级联结构区由5个周期的电子势垒区、吸收区和空穴势垒区组成；N型接触层由100个周期的InAs（2.4 nm）/GaSb（3.6 nm）超晶格和20 nm厚的InAs层组成，掺杂浓度为2×10^{18} cm^{-3}。外延片样品采用分子束外延技术在n型GaSb（001）衬底上使用As源和Sb源生长，将生长的样品进行标准化光刻和蚀刻制备成方形台面结构。方形台面的尺寸为300 μm×300 μm。P型和N型欧姆接触电极都采用Ti/Au金属。

2 实验结果

2.1 暗电流测试

图2是从77 K到300 K温度范围内的变偏压器件暗电流密度曲线，当偏置电压是−20 mV时，在77 K、160 K和300 K时，暗电流密度分别为1.91×10^{-7} A/cm^2、1.95×10^{-5} A/cm^2和4.3×10^{-2} A/cm^2。图2中低温特定正偏压范围内可以观察到负微分电阻效应，并且呈现了与温度相关的趋势。根据暗电流密度的数据，可以计算得到零偏动态电阻与面积的乘积R_0A。例如，在77 K、160 K和300 K时，R_0A分别为2.68×10^4 $\Omega\cdot cm^2$、1.02×10^3 $\Omega\cdot cm^2$和0.44 $\Omega\cdot cm^2$。

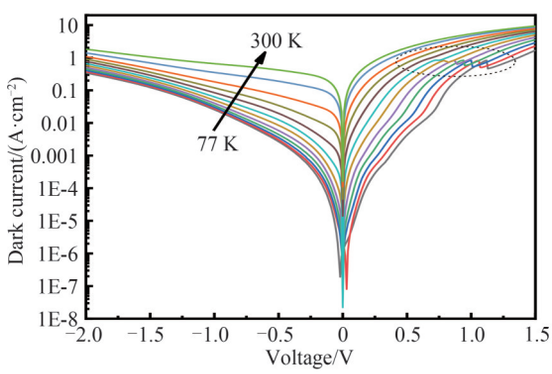

图2 77 K到300 K的暗电流密度曲线

Fig. 2 The dark current density curves from 77 K to 300 K

为了对暗电流机制进行分析，做出如图3所示的温度从77 K到300 K时的暗电流密度对1 000/T（温度）的依赖关系，即Arrhenius曲线。从Arrhenius图可知，在180～300 K之间器件的激活能为279 meV。对于T2SL探测器来说，50%截止波长非常接近超晶格吸收区的有效带隙，即电子基态能级和重空穴基态能级之间的差。而从图4（a）可以得到在300 K时器件50%截止波长是4.88 μm，对应的有效带隙是254 meV。可见激活能非常接近有效带隙的值，这意味着在180到300 K温度范围内扩散暗电流占暗电流的主导地位。

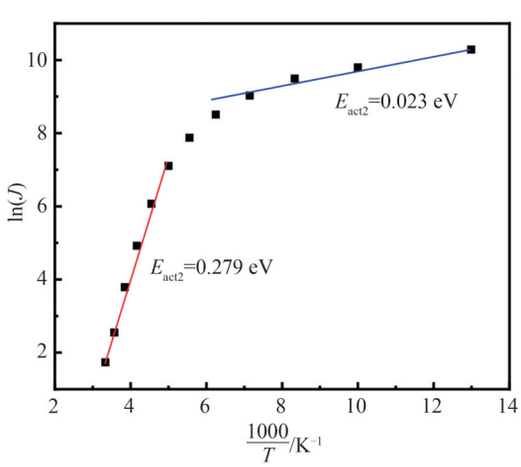

图3 暗电流密度在77 K到300 K之间的Arrhenius图

Fig. 3 The Arrhenius plot of the measured dark current density between 77 K and 300 K

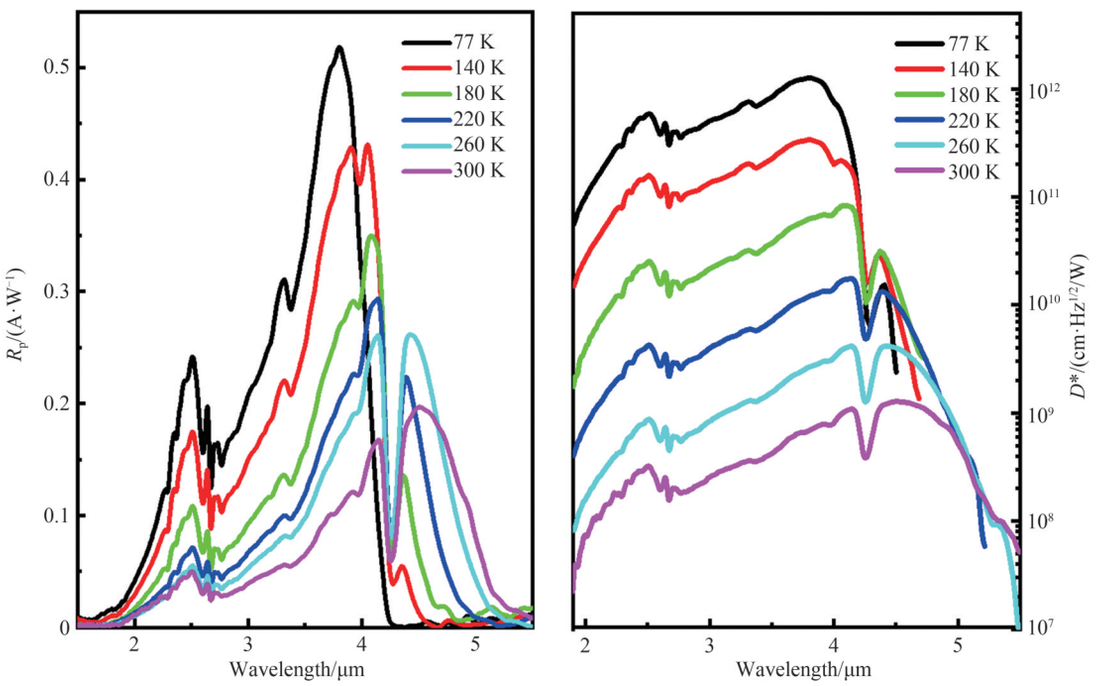

(a) The responsivity of the device from 77 K to 300 K when the bias voltage is 0 V

(b) The detectivity D^* from 77 K to 300 K when the bias voltage is 0 V

图4 当偏置电压为0 V时，器件从77 K到300 K下的响应率和探测率D^*

Fig. 4 The responsivity and the detectivity D^* of the device from 77 K to 300 K when the bias voltage is 0 V

这是因为采用了带间级联结构，对于其他结构的T2SL探测器，在类似的温度范围内的暗电流通常以产生-复合暗电流为主。但在77 K到140 K左右的温度范围内，测量得到的激活能只有23 meV左右。该段的暗电流机制尚不清楚，其中一个猜测是测量得到的暗电流结果可能包括了暗电流和背景辐照导致的光电流。

2.2 响应率与探测率光谱

实验中采用Bruker Vertex 70傅里叶红外光谱仪测试带间级联探测器的光谱，通过将黑体温度设置在800 K校准得到光响应谱。图4是77～300 K温度范围内零偏压时的响应率和探测率谱。ICIP的探测率D^*可以通过以下公式来计算[29]

$$D^* = \frac{R_P}{\sqrt{2K_bT/R_dA + 2K_bT/R_0A}} \tag{1}$$

式中，R_P是响应率，K_b是玻尔兹曼常数，T是温度，R_dA是动态电阻与面积的乘积，R_0A是零偏时的动态电阻与面积乘积，结果在图4(b)中呈现。在77 K时，50% 截止波长为4.02 μm，器件的探测波长非常接近我们的设计，峰值响应波长为3.79 μm，对应的峰值响应率为0.52 A/W，探测率D^*为1.26×10^{12} cm·Hz$^{1/2}$/W。在300 K时，器件的50% 截止波长红移到了4.88 μm，峰值响应波长红移到了4.47 μm，对应的峰值响应率为0.20 A/W，探测率D^*为1.28×10^{9} cm·Hz$^{1/2}$/W。

3 负微分电阻效应分析

2.1节中提到，77 K到220 K温度范围内的暗电流中可以观察到负微分电阻效应(NDR)。在77 K时，当偏置电压约为1.12～1.13 V时，表现出NDR效应；在100 K时，出现NDR效应的偏置电压转移到了1.05～1.08 V；到200 K时，NDR效应的电压范围变为0.72～0.75 V；而当温度升到220 K时，峰值暗电流与谷值暗电流重合在0.66 V处。很明显，出现NDR效应的偏压随温度变化而变化，即器件中存在共振隧穿现象且隧穿条件随温度的变化而变化。

图5呈现了NDR效应的峰值暗电流(I_P)、谷值暗电流(I_V)和峰谷电流比(Peak-to-Valley Current Ratio，PVCR)随温度的变化曲线，PVCR是共振隧穿条件满足程度的指标。在77 K时，I_P约为7.44×10^{-4} A，I_V为

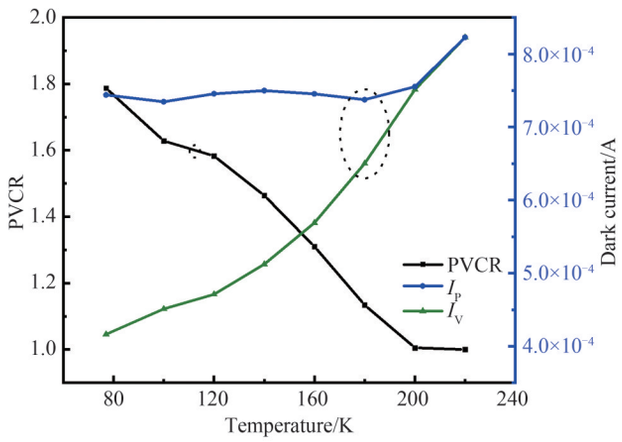

图5　77 K到220 K下的峰值暗电流（I_P）、谷值暗电流（I_V）以及峰谷电流比（PVCR）

Fig. 5　The peak dark current (I_P), the valley dark current (I_V), and the peak-to-valley current ratio (PVCR) from 77 K to 220 K

4.16×10^{-4} A，PVCR计算得1.79。在160 K时，I_P约为7.45×10^{-4} A，I_V是5.69×10^{-4} A，PVCR变成1.31。在220 K时，I_P几乎等于I_V，约为8.23×10^{-4} A，此时PVCR变为1，观察不到NDR效应。从图5中可以看出，随着温度的升高，I_P基本不变，I_V变大，PVCR值降低。暗电流可以表示为

$$I_d(V)=ev(V)n(V)A \tag{2}$$

式中，e为电子电荷，$v(V)$为平均电子漂移速度，A为探测器面积，$n(V)$为产生暗电流的电子浓度。$n(V)$可以表示为[30]

$$n(V)=\int N(E)f(E)T(E,V)\mathrm{d}E \tag{3}$$

式中，$N(E)$为态密度，$f(E)$为Fermi-Dirac分布函数，E为能量态，$T(E,V)$为隧穿概率。在本实验中，器件的隧穿机制共有两种。一种是共振隧穿机制，另一种是通过电子势垒区的隧穿机制。波谷处的暗电流I_V主要是通过带间级联结构中势垒的隧穿暗电流。当温度升高时，$N(E)$和$f(E)$的乘积增大，而隧穿概率$T(E,V)$与能态成指数正比关系，即$T(E,V)$随温度升高指数升高，所以$n(V)$急速升高，因此谷点处的暗电流会随着温度的升高而增加。而在NDR峰值处的暗电流包含了两种机制的暗电流，由两种隧穿机制共同决定了暗电流的变化。根据负微分电阻效应的原理，此处共振隧穿电流达到最大，继续升高偏压则不再满足共振隧穿条件，暗电流随之减小。为了简化模型，通常将共振隧穿电流的隧穿概率$T(E,V)$视为一个常数。温度升高时，满足共振隧穿条件时的$N(E)$和$f(E)$的乘积减小，$n(V)$减小，导致共振隧穿暗电流的减小。在暗电流的结果中可以观察到I_P基本不随温度变化，这可能是因为随着温度的升高共振隧穿暗电流的减小量与通过势垒的暗电流的增大量基本相等。相应地，在较高的温度下，基本不变的I_P和升高的I_V导致了PVCR的减小，最终使PVCR减小到1，不再观察到负微分电阻效应。

4　结论

本文设计并制备了一种采用T2SL材料的带间级联结构的中波红外光电探测器。在77 K时，50%截止波长是4.02 μm，0 V峰值探测率为1.26×10^{12} cm·Hz$^{1/2}$/W。在300 K时，峰值探测率达到1.28×10^{9} cm·Hz$^{1/2}$/W，50%截止波长是4.88 μm，与其他采用带间级联结构制备的更短波长的探测器达到相同探测率水平。在180～300 K的温度范围内，器件的暗电流主要由扩散电流而不是产生复合电流主导。在77～220 K温度范围内的暗电流曲线中也观察到负微分电阻（NDR）效应。结果表明，具有带间级联结构的T2SL探测器可以进行高温工作，特别是在中波长范围内。

参考文献

[1] SMITH D L, MAILHIOT C. Proposal for strained type Ⅱ superlattice infrared detectors [J]. Journal of Applied Physics, 1987, 62(6): 2545-2548.

[2] ZHANG Y, MA W, HUANG J, et al. Pushing detection wavelength toward 1 μm by type II InAs/GaAsSb superlattices with AlSb insertion layers[J]. IEEE Electron Device Letters, 2016, 37(9): 1166-1169.

[3] HUANG J, MA W, WEI Y, et al. How to use type Ⅱ InAs/GaSb superlattice structure to reach detection wavelength of 2-3 μm [J]. IEEE Journal of Quantum Electronics, 2012, 48(10): 1322-1326.
[4] HOANG A M, CHEN G, HADDADI A, et al. Demonstration of shortwavelength infrared photodiodes based on type-Ⅱ InAs/GaSb/AlSb superlattices [J]. Applied Physics Letters, 2012, 100(21): 211101.
[5] HUANG J, MA W, ZHANG Y, et al. Narrow-band type Ⅱ superlattice photodetector with detection wavelength shorter than 2 μm [J]. IEEE Photonics Technology Letters, 2015, 27(21): 2276-2279.
[6] ZHOU X, LI D, HUANG J, et al. Mid-wavelength type Ⅱ InAs/GaSb superlattice infrared focal plane arrays [J]. Infrared Physics & Technology, 2016, 78: 263-267.
[7] POUR S A, HUANG E K, CHEN G, et al. High operating temperature midwave infrared photodiodes and focal plane arrays based on type-Ⅱ InAs/GaSb superlattices [J]. Applied Physics Letters, 2011, 98(14): 143501.
[8] GAUTAM N, MYERS S, BARVE A V, et al. High operating temperature interband cascade midwave infrared detector based on type-Ⅱ InAs/GaSb strained layer superlattice [J]. Applied Physics Letters, 2012, 101(2): 021106.
[9] YE H, LI L, LOTFI H, et al. Molecular beam epitaxy of interband cascade structures with InAs/GaSb superlattice absorbers for long-wavelength infrared detection [J]. Semiconductor Science and Technology, 2015, 30(10): 105029.
[10] GAUTAM N, KIM H S, KUTTY M N, et al. Performance improvement of longwave infrared photodetector based on type-Ⅱ InAs/GaSb superlattices using unipolar current blocking layers [J]. Applied Physics Letters, 2010, 96(23): 231107.
[11] TING D Z Y, HILL C J, SOIBEL A, et al. A high-performance long wavelength superlattice complementary barrier infrared detector [J]. Applied Physics Letters, 2009, 95(2): 023508.
[12] HUANG J, MA W, ZHANG Y, et al. Impact of band structure of Ohmic contact layers on the response feature of p-i-n very long wavelength type Ⅱ InAs/GaSb superlattice photodetector [J]. Applied Physics Letters, 2015, 106(26): 263502.
[13] HOFFMAN D, NGUYEN B M, HUANG E K, et al. The effect of doping the M-barrier in very long-wave type-Ⅱ InAs/GaSb heterodiodes [J]. Applied Physics Letters, 2008, 93(3): 031107.
[14] MAIMON S, WICKS G W. nBn detector, an infrared detector with reduced dark current and higher operating temperature [J]. Applied Physics Letters, 2006, 89(15): 151109.
[15] KLIPSTEIN P C, AVNON E, AZULAI D, et al. Type Ⅱ superlattice technology for LWIR detectors [C]. SPIE, 2016, 9819: 98190T.
[16] NGUYEN B M, RAZEGHI M, NATHAN V, et al. Type-Ⅱ M structure photodiodes: an alternative material design for mid-wave to long wavelength infrared regimes [C]. SPIE, 2007, 6479: 64790S.
[17] GAUTAM N, MYERS S, BARVE A V, et al. Barrier engineered infrared photodetectors based on type-Ⅱ InAs/GaSb strained layer superlattices [J]. IEEE Journal of Quantum Electronics, 2013, 49(2): 211-217.
[18] TIAN Z, HINKEY R T, YANG R Q, et al. Interband cascade infrared photodetectors with enhanced electron barriers and p-type superlattice absorbers [J]. Journal of Applied Physics, 2012, 111(2): 024510.
[19] YANG R Q. Infrared laser based on intersubband transitions in quantum wells [J]. Superlattices and Microstructures, 1995, 17(1): 77-83.
[20] JIANG Y, LI L, YANG R Q, et al. Type-Ⅰ interband cascade lasers near 3.2 μm [J]. Applied Physics Letters, 2015, 106(4): 041117.
[21] LI J V, YANG R Q, HILL C J, et al. Interband cascade detectors with room temperature photovoltaic operation [J]. Applied Physics Letters, 2005, 86(10): 101102.
[22] YANG R Q, TIAN Z, CAI Z, et al. Interband-cascade infrared photodetectors with superlattice absorbers [J]. Journal of Applied Physics, 2010, 107(5): 054514.
[23] GAUTAM N, MYERS S, BARVE AV, et al. High operating temperature interband cascade midwave infrared detector based on type-Ⅱ InAs/GaSb strained layer superlattice [J]. Applied Physics Letters, 2012, 101(2): 021106.
[24] TIAN Z B, GODOY S E, KIM H S, et al. High operating temperature interband cascade focal plane arrays [J]. Applied Physics Letters, 2014, 105(5): 051109.
[25] CHAI X, ZHOU Y, XU Z, et al. Mid-wavelength interband cascade infrared photodetectors with two and three stages [J]. Infrared Physics & Technology, 2020, 107: 103292.
[26] ZHOU Y, CHAI X, TIAN Y, et al. Studies on InAs/GaAsSb mid-wavelength interband cascade infrared focal plane arrays[J]. Journal of Infrared and Millimeter Waves, 2019, 38(6): 745-750.
[27] BADER A, ROTHMAYR F, KHAN N, et al. Interband cascade infrared photodetectors based on Ga-free InAs/InAsSb superlattice absorbers [J]. Applied Physics Letters, 2022, 121(4): 041104.
[28] LEI L, LI L, YE H, et al. Long wavelength interband cascade infrared photodetectors operating at high temperatures [J]. Journal of Applied Physics, 2016, 120(19): 193102.
[29] YANG R Q. Shot and Johnson noises in interband cascade infrared photodetectors [J]. Applied Physics Letters, 2022,

121(5): 051105.

[30] SU X H, CHAKRABARTI S, STIFF-ROBERTS A D, et al. Quantum dot infrared photodetector design based on double-barrier resonant tunnelling [J]. Electronics Letters, 2004, 40(17): 1082-1083.

Mid Wavelength Interband Cascade Photodetector with Type Ⅱ Superlattice Absorber (Invited)

XUE Ting[1,2], HUANG Jianliang[1,2], YAN Shaolong[1,2], ZHANG Yanhua[1,2], MA Wenquan[1,2]

(1 *Key Laboratory of Semiconductor Materials Science, Institute of Semiconductors, Chinese Academy of Sciences, Beijing* 100083, *China*)

(2 *Center of Materials Science and Opto-electronic Engineering, University of Chinese Academy of Sciences, Beijing* 100049, *China*)

Abstract: To reduce the cryogenic cooling cost for high operating temperature applications, the dark current of infrared photodetectors need to be further reduced. Many methods have been proposed such as inserting unipolar-barrier, complementary barriers, the M-structure, and double heterostructures. The Interband Cascade Infrared Photodetectors (ICIP), originally arising from the interband cascade laser, has also been tried. The ICIP structure consists of high bandgap AlSb material, which can further reduce the dark current. Therefore, these features may make high temperature operation possible for ICIPs, especially for the mid wavelength range.

This work investigates the ICIP for mid wavelength operation. The ICIP is designed as a p-i-n type. Specifically, the i region is composed of a 5-stage interband cascade structure. Each cascade stage consists of an electron-barrier (eB) layer, an absorber layer, and a hole-barrier (hB) layer, and this sequence repeats five times. The photogenerated electrons in one absorber layer should first pass through the hB layer by optical phonon assisted stepwise transport. The carriers, which arrive at the hole states of the eB layer, finally tunnel to the next absorber layer. Consequently, the energy levels of the eB and the hB layer should be equidistributed. In other words, the energy difference between adjacent levels should be comparable to the optical phonon energy, about 30 meV.

The absorber layer of each period is designed as 0.5 μm thick InAs (2.4 nm)/GaSb (3.6 nm) SLs, which has an expected cut-off wavelength of around 4.28 μm. The hB layer is made up of 8 InAs QWs, separated by AlSb barrier layers. For the eB layer, it consists of AlSb(2.1 nm)/GaSb(5.3 nm)/AlSb(2.1 nm)/GaSb(7.5 nm)/AlSb(2.1 nm). The calculated energy separation between adjacent levels is close to the optical phonon energy. The sample is grown on an n-type GaSb (001) substrate by molecular beam epitaxy. After the growth, an array mesa was formed using standard photolithography and dry-etched.

We measured the temperature-dependent dark current to reveal the dark current mechanism of the device. The dark current of the device is dominated by the diffusion current instead of the generation-recombination current for the temperature range between 180 K and 300 K, as seen from the Arrhenius plot. The spectral responsivity is measured by calibrating the photocurrent spectrum with the blackbody response with the blackbody source temperature set at 800 K. We calculated the detectivity of the device. At 77 K, the 50% cutoff wavelength is 4.02 μm and the detectivity D^* is 1.26×10^{12} cm·Hz$^{1/2}$/W for the peak wavelength of 3.79 μm at 0 V. At 300 K, the 50% cutoff wavelength is 4.88 μm and the D^* is 1.28×10^{9} cm·Hz$^{1/2}$/W for the peak response wavelength of 4.47 μm at 0 V. We also observed the Negative Difference Resistance (NDR) effect in our device. The NDR effect can be seen in the dark current curves from 77 K to 220 K. The I_P (the NDR peak point current) has almost no change while the I_V (the NDR valley point current) increases, and therefore the Peak-to-Valley Current Ratio (PVCR) (I_P/I_V) decreases with increasing temperature. There are two parts of the tunneling process arising from the interband cascade structures: tunneling through the electron barriers and resonant tunneling. As the dark current equation, $n(V)$ has a strong influence on the dark current, which is determined by the product of the density of states $N(E)$, and the Fermi-Dirac distribution function $f(E)$, and the tunneling probability $T(E, V)$. At the valley point, the dark current is mainly caused by the barrier tunneling mechanism. For the barrier tunneling current, the product of the density of states and the Fermi-Dirac distribution function

$N(E)f(E)$ increases with elevating the temperature. The tunneling probability, $T(E,V)$, is exponentially proportional to the energy state. That is to say, the $T(E,V)$ at a higher energy state is larger than that at a lower energy state. As a result, the I_V rises. Meanwhile, the $T(E,V)$ of the resonant tunneling dark current can be treated as a constant and the $N(E)f(E)$ decreases, resulting in a drop of resonant tunneling current. The dark current at the NDR peak point (I_P) is caused by the both two tunneling mechanism, leading to an almost constant peak dark current. Correspondingly, an unchanged I_P and an increased I_V lead to a smaller PVCR for a higher temperature.

Key words: Semiconductor photodetector; Mid wavelength; Molecular beam epitaxy; Interband cascade photodetector; InAs/GaSb superlattices

OCIS Codes: 040.3060; 040.5160; 160.6000

Foundation item: National Natural Science Foundation of China (No. 61874103)